



Multiple extremely flat bands in twisted bilayer binary materials at large twist angles induced by atomic reconstruction

Dawei Kang ^{1,*}, Zhaowu Wang ², and Zheng-wei Zuo¹¹*School of Physics and Engineering, Henan University of Science and Technology, Luoyang 471023, China*²*School of Science, Hebei University of Technology, Tianjin 300401, China*

(Received 5 May 2023; accepted 7 August 2023; published 14 August 2023)

Flat bands in twisted bilayer two-dimensional materials present a platform for investigating exotic phenomena. However, achieving flat bands typically necessitates small twist angles, resulting in large moiré superlattices that increase experimental complexity and hinder compact device integration. In this work, we discovered that multiple flat bands with extremely low bandwidth can form in twisted bilayer binary materials, such as AlN and GaN, at large twist angles. The atomic reconstruction, which is most pronounced in AlN and GaN among commonly used two-dimensional materials, can alter the electronic localization position and provide effective barriers among the localized states, playing a crucial role in the formation of these ultraflat bands. Our findings offer a unique approach for generating flat bands at large twist angles.

DOI: [10.1103/PhysRevB.108.075415](https://doi.org/10.1103/PhysRevB.108.075415)

I. INTRODUCTION

Adjusting the twist angle in stacked two-dimensional (2D) materials or integrating 2D materials with distinct lattice constants can result in the formation of a large-scale periodic superlattice, known as a moiré superlattice (MSL) [1]. The emergence of an MSL significantly impacts the band structure, giving rise to flat bands in various systems, such as twisted bilayer graphene [2–4], transition metal dichalcogenides (TMDs) [5–7], and other two-dimensional materials [8–10]. In systems exhibiting flat bands, the ratio between electron correlation and kinetic energy may become more pronounced. Consequently, correlation-related phenomena, such as superconductivity [11–13], correlated insulator [14–17], and ferromagnetism [18,19], have been observed in twisted layered 2D materials.

In twisted bilayer graphene, flat bands emerge at discrete magic angles, with the first magic angle observed experimentally [14] at $\sim 1.1^\circ$. For twisted bilayer TMDs [5], *h*-BN [8], and other semiconductive 2D materials [20], flat bands can be induced by the localization of electronic states at small twist angles within the MSL [5]. Furthermore, in twisted bilayer polar 2D materials, flat bands are predicted to emerge at small twist angles without the constraint of magic angles [10]. The real space scale of the MSL expands significantly at small twist angles, which makes the experimental accessibility more complex and hinders the integration of twisted systems into compact devices. For example, the lattice parameter of twisted bilayer 2D materials with hexagonal symmetry is given by $\lambda = a/\sqrt{2(1-\cos\theta)}$, where a represents the lattice parameter of the primitive cell of the monolayer. In twisted bilayer graphene at the magic twist angle of 1.1° , λ will approach 12.8 nm. Thus, in order to investigate flat bands at large twist

angles, Xu *et al.* [21] used several commonly studied 2D materials to construct an MSL at 7.34° . Among these studied 2D materials, flat bands with bandwidths smaller than 3 meV were discovered in twisted bilayer In_2Se_3 . Then, Tao *et al.* [22] attributed the origin of this kind of flat bands to the barrier height that effectively isolates the couplings of localized states. Li *et al.* [23] found that the ferroelectric alignment between layers in twisted bilayer In_2Se_3 can also have impact on the flat bandwidth. However, the flat bands at large twist angles are still rarely discovered in twisted 2D materials. The underlying mechanism of the localization of electronic states at large twist angles are still under debate.

In this study, we discovered multiple flat bands with bandwidths ~ 1 meV in twisted bilayer binary materials, such as GaN and AlN, at a large twist angle of 7.34° . The significant atomic reconstruction takes place because of the large energy difference among the local stackings in an MSL. Atomic reconstruction contributes to the enlargement of specific local stacking with minimum stacking energy, which plays a crucial role in the flattening of these multiple bands. Intriguingly, the enlargement of particular local stacking at large twist angles is a more pronounced phenomenon in twisted bilayer AlN and GaN compared to other commonly used 2D materials, such as twisted bilayer MoS_2 and BN. Therefore, our findings offer a unique approach for generating flat bands at large twist angles.

II. COMPUTATIONAL DETAILS

The atomic reconstruction and electronic structure calculations are performed by the Vienna Ab initial Simulation Package (VASP) [24–26]. The Kohn-Sham orbitals are expanded by the plane-wave basis with a cutoff of 500 eV. The interaction between core electrons and valence electrons are treated by the projected augmented plane-wave method. The generalized gradient approximation (GGA) within the Perdew-Burke-Ernzerhof (PBE) functional form is employed

*kdwsdu@163.com

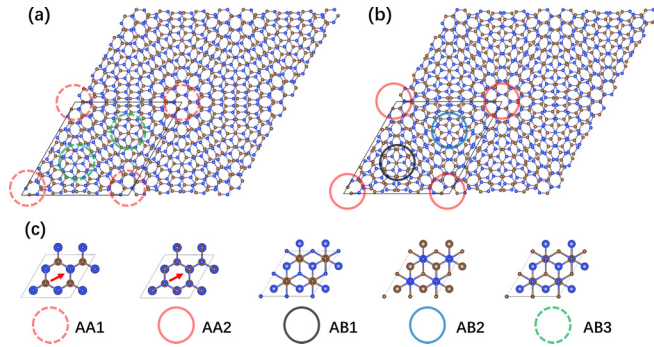


FIG. 1. The twisted bilayer binary 2D materials in (a) alpha and (b) beta phases. The grey and blue spheres represent the two atom species A and B in binary 2D materials. (c) The high-symmetry stackings emerging in the MSLs highlighted by colored circles. The radii of the atoms in the top layer are set to be smaller than those in the bottom layer to visually distinguish different high-symmetry stackings.

for the exchange-correlation energy. The structure relaxation is performed until the residual forces are less than $0.01 \text{ eV}/\text{\AA}$. Hereafter, we mention the twisted bilayer system with or without structural relaxation as relaxed or unrelaxed system. The DFT-D2 method is adopted to correct the van der Waals interactions. A vacuum spacing with more than 15 \AA perpendicular to the two-dimensional surface is used to avoid spurious interactions between repeated units.

The alpha phase as shown in Fig. 1(a) can be regarded as rotating one layer in the AA1 stacking bilayer a small angle, while the beta phase as shown in Fig. 1(b) can be regarded as rotating one layer in the AA2 stacking bilayer a small angle. The alpha phase and beta phase are related by rotating one layer by 60° or 180° . The space groups of the alpha and beta phases are $P-6c2$ and $P-62c$, respectively. The five high-symmetry stackings are listed in Fig. 1(c). The AA1 and AB3 stackings emerge in the alpha phase, while the AA2, AB1, and AB3 phases emerge in the beta phase. The high-symmetry stackings of bilayer binary 2D materials with two atom species A and B in Fig. 1(c) can be described as follows. The AA1 stacking can be understood as placing all atoms of one layer directly on top of the atoms of the same species in another layer. AB3 stacking is achieved by shifting the top layer of AA1 stacking by one bond length, as indicated by the red arrow in Fig. 1(c). AA2 stacking can be conceptualized as placing all atoms of one layer on top of the atoms of a different species in another layer. The AB1 and AB2 stackings are achieved by shifting the top layer of AA2 stacking by one and two bond lengths, respectively, along the red arrow in Fig. 1(c).

III. ATOMIC RECONSTRUCTION

The atomic reconstruction of twisted bilayer binary materials which are composed by two species of elements, such as AlN, GaN, BN, MoS₂, SiC, and BP, is initially analyzed. The lattice constants of these six 2D materials are 3.12, 3.24, 2.51, 3.16, 3.12, and 3.21 \AA , respectively. The most significant atomic reconstruction occurs in the beta phase of these twisted binary materials, which is the focus of the subsequent

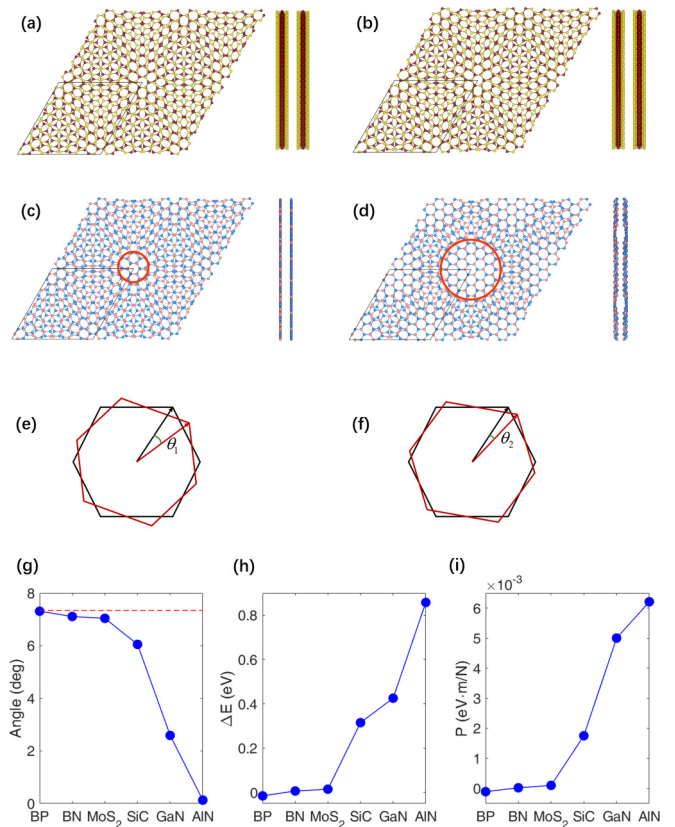


FIG. 2. The top and side views of (a) unrelaxed twisted bilayer MoS₂, (b) relaxed twisted bilayer MoS₂, (c) unrelaxed twisted bilayer AlN, and (d) relaxed twisted bilayer AlN at a twist angle of 7.34° . The grey, yellow, blue, and pink spheres represent Mo, S, N, and Al atoms, respectively. The solid black rhombuses represent the MSLs. The red circles in (c) and (d) indicate the area of the AA2 stacking. (e), (f) The schematics of twist angle variation between the two hexagons at the twist center of AA2 stackings of (e) unrelaxed and (f) relaxed twisted bilayers. (g) The twist angle between the two hexagons at the twist center for relaxed structures of twisted bilayer binary 2D materials studied in this work. The red-dashed line represents the 7.34° twist angle of the initial unrelaxed twisted bilayers. (h) The energy difference between AA2 stacking and the stacking with the second-lowest energy for binary 2D materials studied in this work. The high-symmetry stacking with the second-lowest energy is AB2 stacking. (i) The same with (h) but replacing ΔE with $P = \Delta E/Y$, where Y is the Young's modulus.

analysis (details of constructing commensurate MSLs are presented in Appendix A). Figures 2(a)–2(d) illustrate the atomic structure of the twisted bilayer MoS₂ (tb-MoS₂) MSL and tb-AlN MSL before and after atomic reconstruction. At a large twist angle of 7.34° , there are no apparent displacements in tb-MoS₂ due to atomic reconstruction. However, the atomic reconstruction in tb-AlN is more pronounced, with interlayer interactions leading to substantial corrugations in the relaxed tb-AlN. Notably, the AA2 stacking [indicated by the red circle in Fig. 2(c)] expands to extensive areas, as demonstrated by the red circle in Fig. 2(d). To assess the degree of AA2 stacking expansion, the local twist angle between the two hexagons from the top and bottom layers at the twist center of AA2 stackings is plotted in Fig. 2(e) (unrelaxed structure) and

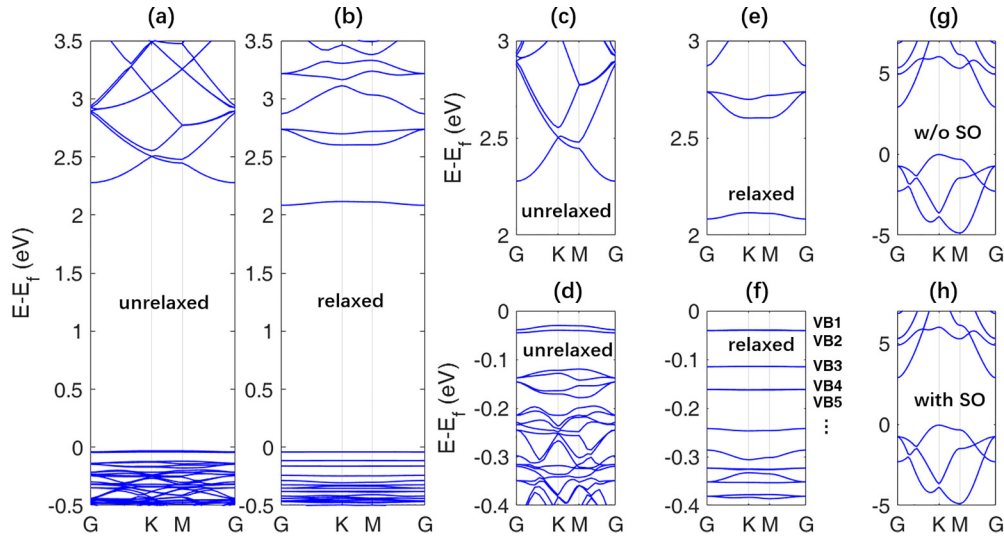


FIG. 3. The band structure of (a) unrelaxed and (b) relaxed tb-AlN at twist angle of 7.34° . Panels (c)–(f) plot the band structures of (c),(d) unrelaxed and (e),(f) relaxed tb-AlN in a narrow energy range. The valence bands are marked as VB n where “ n ” are integers. (g)–(h) plot the band structure of monolayer AlN (g) without and (h) with spin-orbit coupling.

Fig. 2(f) (relaxed structure). The expansion of AA2 stacking is proportional to the deviation of the two local twist angles $\theta_1 - \theta_2$. Note that Figs. 2(e) and 2(f) are schematics to illustrate the local twist angle variation and the twist angle in real materials like tb-AlN may approach near zero. For an unrelaxed twisted bilayer, the initial local twist angle is denoted as $\theta_1 = 7.34^\circ$. After atomic reconstruction, the local twist angle at the twist center of twisted bilayer binary 2D materials studied in this work is illustrated in Fig. 2(g). For tb-BP, tb-BN, and tb-MoS₂, the local twist angles are close to the initial value of 7.34° . However, for tb-SiC, tb-GaN, and tb-AlN, the local twist angles approach smaller values. The local twist angle for tb-AlN even reaches approximately zero. Consequently, the area of AA2 stackings in tb-AlN is significantly enlarged.

To elucidate the expansion of AA2 stackings in tb-GaN and tb-AlN, the stacking energy differences between AA2 stacking and high-symmetry stacking with the second-lowest energy (AB2 stacking in this study) are plotted in Fig. 2(h). Among the six 2D materials studied in this work, AA2 stacking exhibits the lowest stacking energy. The stacking energy, as illustrated in Fig. 2(h), demonstrates an inverse relationship among the six 2D materials with that of the local twist angle, as presented in Fig. 2(g). For AlN, the stacking energy difference reaches approximately 0.8 eV. Therefore, the expansion of AA2 stackings can be effectively interpreted by the energy minimization principle. AlN exhibits the largest stacking energy difference, which results in the most substantial expansion of AA2 stackings to achieve maximal energy gain. Another consideration is that the expansion of AA2 stackings induces lattice distortion. Assuming that lattice distortion is inversely related to Young’s modulus, the defined parameter $P = \Delta E/Y$ [Fig. 2(i)] exhibits a similar dependence as shown in Fig. 2(h). The Young’s modulus $Y = \frac{1}{V_0} \frac{\partial^2 U}{\partial \varepsilon^2} |_{\varepsilon=0}$, where V_0 is the initial volume of the structure, U is the strain energy due to deformation, and ε is the strain. The Young’s modulus of BP [27], BN [28], MoS₂ [29], SiC [28], GaN [28], and

AlN [28] are 146.3, 263.4, 141.5, 179.6, 85.1, and 138.1 N/m, respectively. Note that the prominent atomic reconstruction usually occurs at a very small twist angles for twisted bilayer graphene ($<1^\circ$) [30] and TMD ($<3^\circ$) [31]. Therefore, tb-GaN and tb-AlN provide platforms for studying the electronic response to significant atomic reconstruction at large twist angles.

IV. EFFECT OF ATOMIC RECONSTRUCTION ON FLAT BANDS

The atomic reconstruction discussed above can significantly impact the electronic structure of the twisted bilayer system. In Figs. 3(a)–3(f), the band structures of tb-AlN at a twist angle of 7.34° before and after atomic reconstruction are plotted. The band plots near the bottom conduction band and top valence band become flattened after atomic reconstruction, as shown in Figs. 3(a) and 3(b). To visually distinguish the dense band plots, the band structures are presented within a narrow energy range, as depicted in Figs. 3(c)–3(f). The bottom conduction band flattens after atomic reconstruction, but the bandwidth, as demonstrated in Fig. 3(e), still reaches a substantial value of approximately 30 meV. Interestingly, multiple valence bands become extremely flattened after atomic reconstruction, with a bandwidth of about 1 meV, as shown in Fig. 3(f). For instance, the top valence band labeled by VB1 in Fig. 3(f) has a bandwidth of $W = 1.2$ meV. The on-site Coulomb interaction U in tb-AlN can be estimated as $U = \frac{e^2}{4\pi\epsilon_0\epsilon d}$, where e is the electron charge, ϵ_0 is the vacuum permittivity, ϵ is the relative permittivity, and d is the length scale of the moiré pattern. For tb-AlN at a twist angle of 7.34° , the value of U is ~ 328 meV, with $d = 24.4$ Å and $\epsilon = 1.8$ [32]. The large value of U/W can induce the Mott-insulator transition at half filling. Note that the spacing of flat bands is on the order of 100 meV. The effect of interband effect and the interaction renormalization could be important. The impact of

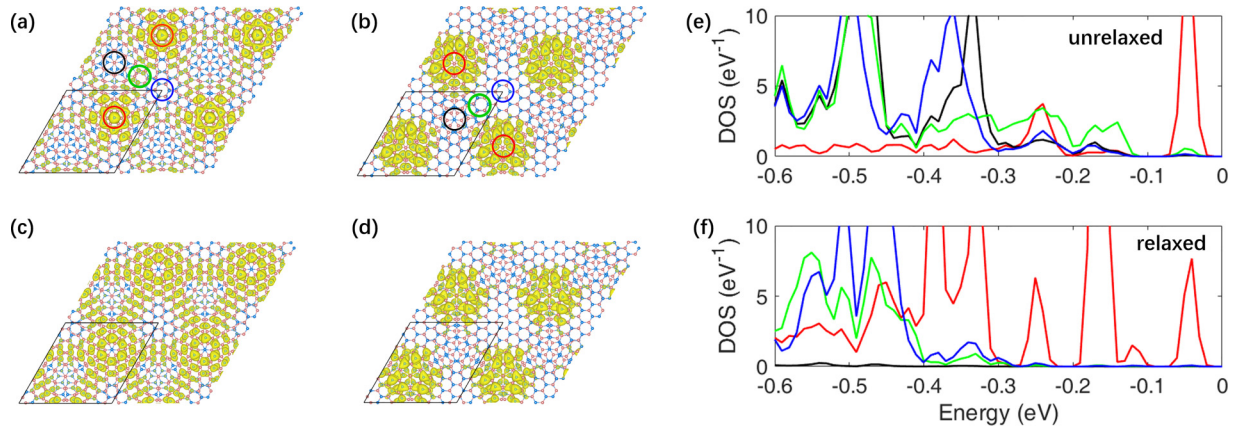


FIG. 4. The charge density of (a), (b) VB1 and (c), (d) VB3 at K point for (a), (c) unrelaxed and (b), (d) relaxed tb-AlN MSL at twist angle of 7.34° . The isosurfaces are $10^{-12} e/\text{\AA}^3$. (e), (f) The projected DOS on the atoms in the colored circles according to (a) and (b) with consistent plot colors.

spin orbit coupling on the band structure of AlN is found to be negligible as shown in Figs. 3(g) and 3(h).

The presence of extremely flat bands can be attributed to the localization of electron states, as demonstrated in Fig. 4, where atomic reconstruction plays a crucial role in inducing the localization. Figures 4(a) and 4(b) present the charge density of the electronic state corresponding to VB1 at the K point in the band plots shown in Figs. 3(d) and 3(f). For the unrelaxed structure, the state primarily localizes at $AB2$ stackings, but the localized states exhibit couplings, as indicated by the remaining charge density in the region enclosed by the green circle in Fig. 4(a). After atomic reconstruction, the state localizes at $AB1$ stackings, as depicted in Fig. 4(b). The localized states exhibit smaller couplings due to the near absence of remaining charge density in the regions interconnecting the localized states. The localization of the state corresponding to VB3, as shown in Figs. 4(c) and 4(d), exhibits a more pronounced transition from “near localization” to “complete localization.” Consequently, atomic reconstruction changes the localization position and makes the state more localized.

The detailed mechanism of the localization transition induced by atomic reconstruction can be analyzed by examining the barrier separating the localized states. The barrier height can be estimated by the difference between the highest energies of the projected density of states (PDOS) on localized states [red circles in Figs. 4(a) and 4(b)] and the connecting region [black, green, and blue circles in Figs. 4(a) and 4(b)]. For the unrelaxed structure, the PDOS on the localized center enclosed by the red circles in Fig. 4(a) exhibits a peak [red curve in Fig. 4(e)] near the valence band maximum (VBM). Although the PDOS on the region enclosed by the black and blue circles in Fig. 4(a) is distant from this red peak, the PDOS on the region enclosed by the green circle in Fig. 4(a) also exhibits a small peak [green curve in Fig. 4(e)] near zero. As a result, the barrier formed along the black, green, and blue circles in Fig. 4(a) has a gap in the center, through which the localized states in Fig. 4(a) can have finite couplings. For the relaxed structure, the PDOS on the localized states enclosed by the red circles in Fig. 4(b) exhibits a peak [red

curve in Fig. 4(f)] close to the VBM. The PDOS on the region enclosed by the black, green, and blue circles in Fig. 4(b) has a noticeable distance from this red peak. It is important to note that the blue circle in Fig. 4(b) is located at the center of $AA2$ stacking, while the green circle is situated at the margin of $AA2$ stacking due to the enlargement of $AA2$ stacking in tb-AlN after atomic reconstruction. The PDOS on the atoms enclosed by green and blue circles exhibits similar curves, as shown in Fig. 4(f). The barrier formed along the black, green, and blue circles in Fig. 4(b) has a well-defined height, which completely separates the localized states. Therefore, the localized states in Fig. 4(b) cannot couple to the neighboring localized states. The completely localized states induce the extremely flat bands, as shown in Fig. 3(f).

The atomic reconstruction can flatten multiple bands in twisted bilayer AlN and GaN. The width of multiple bands can be reduced to extremely low values. In Fig. 5, the bandwidths of valence bands are presented for tb-AlN and tb-GaN at twist angles of 7.34° and 6.01° . After atomic reconstruction, the five valence bands, VB1–VB5, can have a bandwidth of about

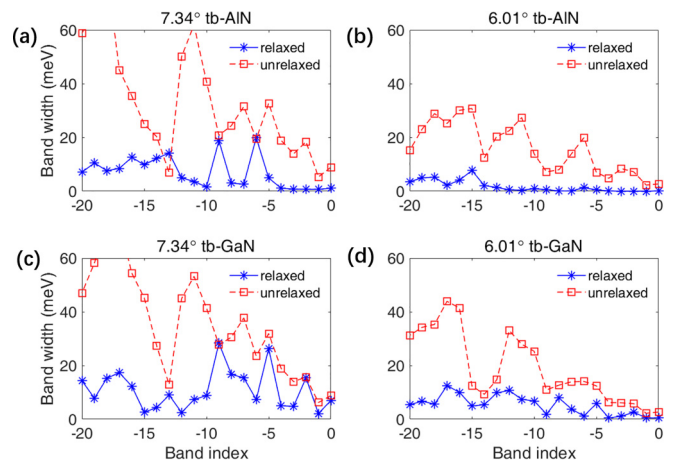


FIG. 5. The bandwidth of the valence band with band index decreasing from zero. The band index “0” represents the top valence band.

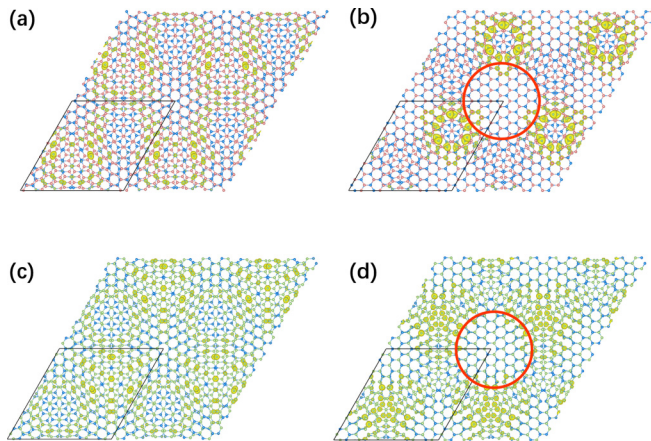


FIG. 6. The charge density of VB7 for (a), (b) tb-AlN and (c), (d) tb-GaN at K point for (a), (c) unrelaxed and (b), (d) relaxed tb-AlN MSL at twist angle of 7.34° . The isosurfaces are $10^{-12} e/\text{\AA}^3$. The blue, pink, and green spheres represent N, Al, and Ga atoms, respectively.

1 meV. When the twist angle reaches 6.01° , the relaxed tb-AlN can have 14 bands with a bandwidth of about 1 meV. The similar bandwidth reduction can be found in tb-GaN at twist angles of 7.34° and 6.01° .

In the case of tb-AlN and tb-GaN at a 6.01° twisted angle, an increased number of valence bands exhibit flattening. For instance, the states of the VB7 band at the K point for tb-AlN and tb-GaN at 6.01° are illustrated in Fig. 6. These states become more localized following structural relaxation. Subsequent to structural relaxation, the AA2 stackings in Figs. 6(b) and 6(d) expand to a larger area (indicated by the red circles) compared to that in Figs. 6(a) and 6(c). This expansion of the AA2 stackings enhances the localization of the states.

V. DISCUSSION

The change of localized position is associated with the energy evolution of states localized at different local stackings. For instance, there is no state distributing at the local stacking denoted by the black circle in Fig. 4(a) due to its energy being below -0.1 eV, as indicated by the black line in the PDOS plot in Fig. 4(e). Postrelaxation, the same local stacking, denoted by the red circle in Fig. 4(b), possesses states due to its energy shifting to a higher energy level of approximately -0.04 eV as shown in Fig. 4(f). In conclusion, the energy of the state has transitioned to a higher energy range. Conversely, the energy of the state corresponding to the local stacking denoted by the red circle in Fig. 4(a) has transitioned to a lower energy range. A qualitative explanation for this energy shift can be inferred as follows: different interlayer interaction forms such as AB1 stacking (where nitrogen atoms from different layers overlap) and AB2 stacking (where aluminium atoms overlap) are present in the local stackings. The energy evolution will exhibit a stacking dependence on atomic reconstructions, including interlayer twisting and interlayer distance (details of qualitative analysis on the energy variation of localized states

are presented in Appendix C). Therefore, the localization position will change accordingly.

The significant energy difference among the high-symmetry stackings that emerge in the twisted bilayers contributes to the notable atomic reconstruction at large twist angles. The stacking with the lowest energy expands over a large area. This expansion can serve as an effective barrier to induce more localized electrons and flat bands. Therefore, if another material exhibits a large energy difference among high-symmetry stackings, leading to prominent atomic reconstruction, similar flat bands may emerge.

VI. CONCLUSION

In conclusion, the effect of atomic reconstruction on flat bands in twisted bilayer binary materials is studied. The large energy differences among the high-symmetry stackings in bilayer AlN and GaN induce the significant atomic reconstruction in the twisted bilayer system at large twist angles. The characteristic of this atomic reconstruction is the enlargement of the AA2 stackings. The atomic reconstruction can change the electronic localization position and provide an effective barrier among the localized states. Therefore, multiple flat bands with extremely lower bandwidth can emerge at large twist angles.

ACKNOWLEDGMENTS

We thank W. Ju for useful discussions on the qualitative analysis of energy variation of localized states. This work was supported by the National Natural Science Foundation of China (Grant No. 11204066) and the Natural Science Foundation of Henan Province (Grant No. 232300420112).

APPENDIX A: CONSTRUCTION OF TWISTED BILAYER HEXAGONAL 2D MATERIALS

The commensurate MSL of twisted bilayer two-dimensional materials with hexagonal symmetry can be considered as stacking two supercells with lattice vectors $(m\vec{a}_1 + n\vec{a}_2, -n\vec{a}_1 + m\vec{a}_2 + \vec{a}_2)$ and $(n\vec{a}_1 + m\vec{a}_2, -m\vec{a}_1 + n\vec{a}_2 + \vec{a}_2)$, where m (n) are integers and \vec{a}_1 (\vec{a}_2) are the lattice vector of the primitive cell of monolayer. The twist angle can be calculated according to $\cos(\theta) = \frac{n^2 + 4mn + m^2}{2(n^2 + mn + m^2)}$.

APPENDIX B: GLOBAL ENERGY MINIMUM OF THE ATOMIC RECONSTRUCTION

The structure characterized by atomic reconstructions is derived through first-principles geometry relaxations. To verify that the final structure, obtained via this relaxation process, corresponds to the structure with the global energy minimum, we scrutinize the atomic reconstruction of twisted bilayer AlN as a representative example. As illustrated in Figs. 7(a) and 7(b), the areas of AB1 and AB2 stackings diminish, while the area of AA2 stacking enlarges, following atomic reconstruction. The formation energy is defined as $\delta E = (E_{\text{bilayer}} - 2E_{\text{monolayer}})/N$, where E_{bilayer} , $E_{\text{monolayer}}$, and N denote the energy of bilayer, the energy of monolayer, and

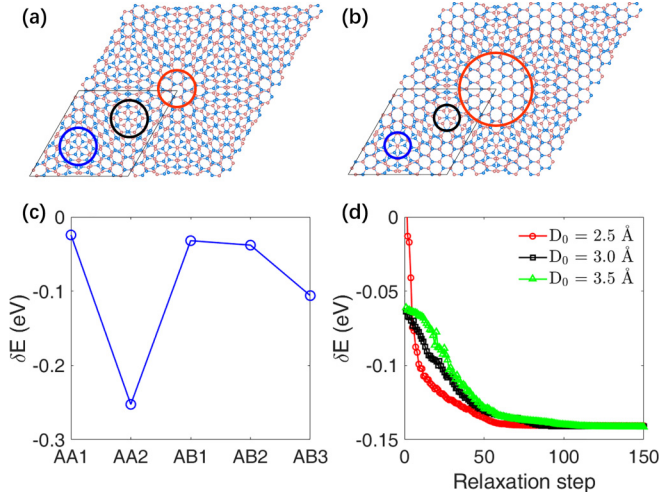


FIG. 7. (a) Unrelaxed twisted bilayer AlN, and (b) relaxed twisted bilayer AlN at twist angle of 7.34° . The blue and pink spheres represent N and Al atoms, respectively. The solid black rhombuses represent the MSLs. The red, blue, and black circles in (a) and (b) indicate the area of the AA2, AB1, and AB2 stackings. (c) The formation energy of bilayer AlN high-symmetry stackings. (d) The formation energy along the relaxation process at different initial interlayer distances.

the total number of atoms in the bilayer system, respectively. The formation energy signifies the energy benefit gained after the creation of the bilayer system. The formation energy of bilayer AlN at high-symmetry stackings is depicted in Fig. 7(c). For the AA2, AB1, and AB2 stackings emerging in Figs. 7(a) and 7(b), the AA2 stacking possesses the lowest formation energy of -0.25 eV, while AB1 and AB2 stackings exhibit higher formation energies of -0.03 and -0.04 eV, respectively. Consequently, the atomic reconstruction of the twisted bilayer AlN optimizes the total energy of the system by augmenting the area of AA2 stacking and reducing the AB1 and AB2 stackings. We also conduct structural relaxation for twisted bilayer AlN at varying initial interlayer distances, leading to the attainment of an identical structure with atomic reconstruction. As demonstrated in Fig. 7(d), the formation energy of the twisted bilayer AlN consistently decreases and converges to -0.14 eV for all three initial interlayer distances of 2.5, 3.0, and 3.5 \AA . Thus, the structure characterized by atomic reconstruction is the structure that represents the global energy minimum.

APPENDIX C: QUALITATIVE ANALYSIS OF ENERGY VARIATION OF LOCALIZED STATES

For high-symmetry stackings, such as AA1 and AA2 configurations, it is feasible to approximate the relative variation in energy using the subsequent Hamiltonian,

$$H = \begin{bmatrix} \varepsilon_1 & t \\ t^* & \varepsilon_2 \end{bmatrix}. \quad (\text{C1})$$

Herein, ε_1 and ε_2 represent the energy levels of atoms A and B, respectively, in the binary 2D materials. The variable t denotes the coupling between atoms from distinct layers.

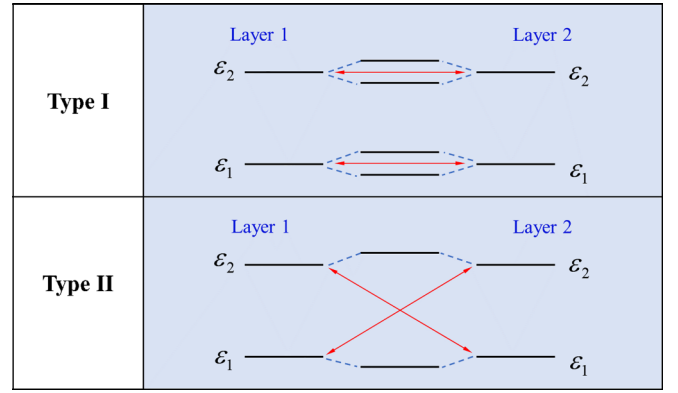


FIG. 8. Schematic of the interlayer interactions, classified as type I and type II. The red arrows depict the interaction of energy levels.

In the case of AA1 stacking, atom A in the upper layer interacts with atom A in the lower layer, and similarly, atom B in the upper layer interacts with atom B in the lower layer. This interaction is considered when taking into account only the nearest neighboring interlayer interactions. Simplifying this by setting $\varepsilon_1 = -E_0$ and $\varepsilon_2 = E_0$, the Hamiltonian can be expressed as follows:

$$H = \begin{bmatrix} -E_0 & t \\ t^* & -E_0 \end{bmatrix}. \quad (\text{C2})$$

Upon diagonalization of H , the subsequent energy levels are obtained:

$$E_1 = -E_0 - |t|, \quad (\text{C3})$$

$$E_2 = -E_0 + |t|. \quad (\text{C4})$$

The energy level ε_1 bifurcates into two levels, and a similar split in the energy level is observed for ε_2 . This division is depicted in Fig. 8 and is classified as type I.

For AA2 stacking, the Hamiltonian can be expressed as follows:

$$H = \begin{bmatrix} -E_0 & t \\ t^* & E_0 \end{bmatrix}. \quad (\text{C5})$$

Upon diagonalizing H , the subsequent energy levels are obtained:

$$E_1 = -\sqrt{E_0^2 + |t|^2}, \quad (\text{C6})$$

$$E_2 = \sqrt{E_0^2 + |t|^2}. \quad (\text{C7})$$

The energy split is demonstrated in Fig. 8 and is classified as type II.

Consequently, the interlayer interaction causes two of the energy levels of AA1 stacking to gravitate towards zero energy, while the interlayer interaction results in the energy levels of AA2 stacking diverging from zero energy. This enables a qualitative approximation of the direction of the energy level shift. For AB1, AB2, and AB3 stackings, the interlayer stackings become more intricate as the vertical projection of atoms from one layer may be located at the hollow site. Furthermore, the next nearest neighboring coupling may become significant, resulting in the coexistence

of type I and type II interlayer interactions. The competition between the type I and type II interactions complicates the qualitative estimation of the energy level shift. Additionally, for the local stackings that emerge in an MSL, the local

twisting and interlayer lattice reconstruction render the local stacking notably different from the high-symmetry stackings, thereby complicating the qualitative estimation of the energy level.

-
- [1] K. Tang and W. Qi, Moiré-pattern-tuned electronic structures of van der Waals Heterostructures, *Adv. Funct. Mater.* **30**, 2002672 (2020).
- [2] R. Bistritzer and A. H. MacDonald, Moiré bands in twisted double-layer graphene, *Proc. Natl. Acad. Sci. USA* **108**, 12233 (2011).
- [3] Z. Song, Z. Wang, W. Shi, G. Li, C. Fang, and B. A. Bernevig, All Magic Angles in Twisted Bilayer Graphene are Topological, *Phys. Rev. Lett.* **123**, 036401 (2019).
- [4] M. J. Park, Y. Kim, G. Y. Cho, and S. Lee, Higher-Order Topological Insulator in Twisted Bilayer Graphene, *Phys. Rev. Lett.* **123**, 216803 (2019).
- [5] M. H. Naik and M. Jain, Ultraflatbands and Shear Solitons in Moiré Patterns of Twisted Bilayer Transition Metal Dichalcogenides, *Phys. Rev. Lett.* **121**, 266401 (2018).
- [6] E. Li, J.-X. Hu, X. Feng, Z. Zhou, L. An, K. T. Law, N. Wang, and N. Lin, Lattice reconstruction induced multiple ultra-flat bands in twisted bilayer WSe₂, *Nat. Commun.* **12**, 5601 (2021).
- [7] L. Xian, M. Claassen, D. Kiese, M. M. Scherer, S. Trebst, D. M. Kennes, and A. Rubio, Realization of nearly dispersionless bands with strong orbital anisotropy from destructive interference in twisted bilayer MoS₂, *Nat. Commun.* **12**, 5644 (2021).
- [8] L. Xian, D. M. Kennes, N. Tancogne-Dejean, M. Altarelli, and A. Rubio, Multiflat bands and strong correlations in twisted bilayer boron nitride: Doping-induced correlated insulator and superconductor, *Nano Lett.* **19**, 4934 (2019).
- [9] J. An and J. Kang, Emergence and tuning of multiple flat bands in twisted bilayer γ -graphyne, *J. Phys. Chem. Lett.* **12**, 12283 (2021).
- [10] X.-J. Zhao, Y. Yang, D.-B. Zhang, and S.-H. Wei, Formation of Bloch Flat Bands in Polar Twisted Bilayers without Magic Angles, *Phys. Rev. Lett.* **124**, 086401 (2020).
- [11] Y. Cao, V. Fatemi, S. Fang, K. Watanabe, T. Taniguchi, E. Kaxiras, and P. Jarillo-Herrero, Unconventional superconductivity in magic-angle graphene superlattices, *Nature (London)* **556**, 43 (2018).
- [12] L. Balents, C. R. Dean, D. K. Efetov, and A. F. Young, Superconductivity and strong correlations in Moiré flat bands, *Nat. Phys.* **16**, 725 (2020).
- [13] P. Törmä, S. Peotta, and B. A. Bernevig, Superconductivity, superfluidity and quantum geometry in twisted multilayer systems, *Nat. Rev. Phys.* **4**, 528 (2022).
- [14] Y. Cao, V. Fatemi, A. Demir, S. Fang, S. L. Tomarken, J. Y. Luo, J. D. Sanchez-Yamagishi, K. Watanabe, T. Taniguchi, E. Kaxiras, R. C. Ashoori, and P. Jarillo-Herrero, Correlated insulator behaviour at half-filling in magic-angle graphene superlattices, *Nature (London)* **556**, 80 (2018).
- [15] M. Xie and A. H. MacDonald, Nature of the Correlated Insulator States in Twisted Bilayer Graphene, *Phys. Rev. Lett.* **124**, 097601 (2020).
- [16] A. Ghiotto, E.-M. Shih, G. S. S. G. Pereira, D. A. Rhodes, B. Kim, J. Zang, A. J. Millis, K. Watanabe, T. Taniguchi, and J. C. Hone, Quantum criticality in twisted transition metal dichalcogenides, *Nature (London)* **597**, 345 (2021).
- [17] H. Pan and S. D. Sarma, Interaction-Driven Filling-Induced Metal-Insulator Transitions in 2D Moiré Lattices, *Phys. Rev. Lett.* **127**, 096802 (2021).
- [18] A. L. Sharpe, E. J. Fox, A. W. Barnard, J. Finney, K. Watanabe, T. Taniguchi, M. A. Kastner, and D. Goldhaber-Gordon, Emergent ferromagnetism near three-quarters filling in twisted bilayer graphene, *Science* **365**, 605 (2019).
- [19] N. Bultinck, S. Chatterjee, and M. P. Zaletel, Mechanism for Anomalous Hall Ferromagnetism in Twisted Bilayer Graphene, *Phys. Rev. Lett.* **124**, 166601 (2020).
- [20] D. Kang, Z.-w. Zuo, W. Ju, and Z. Wang, Emergence of flat bands in twisted bilayer C₃N induced by simple localization and destructive interference, *Phys. Rev. B* **107**, 085425 (2023).
- [21] Q. Xu, Y. Guo, and L. Xian, Moiré flat bands in twisted 2D hexagonal vdW materials, *2D Mater.* **9**, 014005 (2021).
- [22] S. Tao, X. Zhang, J. Zhu, P. He, S. A. Yang, Y. Lu, and S.-H. Wei, Designing ultra-flat bands in twisted bilayer materials at large twist angles: Theory and application to two-dimensional indium selenide, *J. Am. Chem. Soc.* **144**, 3949 (2022).
- [23] C. F. Li, W. J. Zhai, Y. Q. Li, Y. S. Tang, J. H. Zhang, P. Z. Chen, G. Z. Zhou, X. M. Cui, L. Lin, Z. B. Yan, X. K. Huang, X. P. Jiang, and J. M. Liu, Extremely flat band in antiferroelectric bilayer α -In₂Se₃ with large twist-angle, *New J. Phys.* **23**, 083019 (2021).
- [24] P. E. Blöchl, Projector augmented-wave method, *Phys. Rev. B* **50**, 17953 (1994).
- [25] G. Kresse and J. Furthmüller, Efficient iterative schemes for *ab initio* total-energy calculations using a plane-wave basis set, *Phys. Rev. B* **54**, 11169 (1996).
- [26] G. Kresse and D. Joubert, From ultrasoft pseudopotentials to the projector augmented-wave method, *Phys. Rev. B* **59**, 1758 (1999).
- [27] T. V. Vu, A. I. Kartamyshev, N. V. Hieu, T. D. H. Dang, S.-N. Nguyen, N. A. Poklonski, C. V. Nguyen, H. V. Phuc, and N. N. Hieu, Structural, elastic, and electronic properties of chemically functionalized boron phosphide monolayer, *RSC Adv.* **11**, 8552 (2021).
- [28] M.-Q. Le, Atomistic study on the tensile properties of hexagonal AlN, BN, GaN, InN and SiC sheets, *J. Comput. Theor. Nanosci.* **11**, 1458 (2014).
- [29] N. K. Nepal, L. Yu, Q. Yan, and A. Ruzsinszky, First-principles study of mechanical and electronic properties of bent monolayer transition metal dichalcogenides, *Phys. Rev. Mater.* **3**, 073601 (2019).
- [30] H. Yoo, R. Engelke, S. Carr, S. Fang, K. Zhang, P. Cazeaux, S. H. Sung, R. Hovden, A. W. Tsien, and T. Taniguchi, Atomic

- and electronic reconstruction at the van der Waals interface in twisted bilayer graphene, *Nat. Mater.* **18**, 448 (2019).
- [31] A. Weston, Y. Zou, V. Enaldiev, A. Summerfield, N. Clark, V. Zólyomi, A. Graham, C. Yelgel, S. Magorrian, and M. Zhou, Atomic reconstruction in twisted bilayers of transition metal dichalcogenides, *Nat. Nanotechnol.* **15**, 592 (2020).
- [32] M. Beshkova and R. Yakimova, Properties and potential applications of two-dimensional AlN, *Vacuum* **176**, 109231 (2020).